



# An efficient approximate numerical method for modeling contact of materials with distributed inhomogeneities



Qinghua Zhou<sup>a,b</sup>, Xiaoqing Jin<sup>a,\*</sup>, Zhanjiang Wang<sup>a</sup>, Jiaxu Wang<sup>a</sup>, Leon M. Keer<sup>b</sup>, Qian Wang<sup>a,b,\*</sup>

<sup>a</sup> State Key Laboratory of Mechanical Transmission, Chongqing University, Chongqing 400030, China

<sup>b</sup> Department of Mechanical Engineering, Northwestern University, Evanston, IL 60208, USA

## ARTICLE INFO

### Article history:

Received 31 May 2013

Received in revised form 6 May 2014

Available online 18 June 2014

### Keywords:

Distributed inhomogeneities

Equivalent inclusion method

Volumetric stress integral

Rolling contact fatigue

## ABSTRACT

This research explores the influence of distributed non-interpenetrating inhomogeneities on the contact of inhomogeneous materials via a new efficient numerical model based on Eshelby's Equivalent Inclusion Method. The half-space contact of a sphere with an inhomogeneous material is considered, and the solutions take into account interactions between all inhomogeneities. The efficiency and solution accuracy of the proposed method are demonstrated through comparative studies with those of an existing numerical method and the finite element method. The influence of spatial inhomogeneity orientations on the contact elastic field is investigated and parametric studies are conducted for the effect of arbitrarily distributed inhomogeneities on the stress field of the materials. The significance of the influences of inhomogeneity distribution parameters on the inverse volumetric stress integral is quantified and the corresponding data are fitted into selected several formulas as a step towards understanding the rolling contact fatigue life of the materials.

© 2014 Elsevier Ltd. All rights reserved.

## 1. Introduction

An inhomogeneity is a region having properties different from those of the surrounding material (matrix) (Mura, 1993). Inhomogeneities often arbitrarily appear in many engineering materials. When such a material is under external loading, inhomogeneities can cause incompatibility of deformations in the inhomogeneities and the matrix, as well as localized stress concentrations (Leroux et al., 2010), thus influencing the mechanical and physical properties of the material (Murakami and Endo, 1994). These stress concentrations affect the service life of the material (Kuo, 2007). Therefore, it is important to analyze the inhomogeneous disturbance quantitatively and to understand the failure mechanisms induced by inhomogeneities.

The complex analysis as an efficient analytical method was first proposed and applied to two-dimensional (2D) plane elasticity cases by Muskhelishvili in the 1950s (Muskhelishvili, 1953). This work inspired many other studies on 2D heterogeneous problems (Gong and Meguid, 1993; Horii and Nemat-Nasser, 1985; Kushch

\* Corresponding authors. Tel.: +86 847 467 7510; fax: +86 847 467 3427 (X. Jin). Address: State Key Laboratory of Mechanical Transmission, Chongqing University, Chongqing 400030, China (Q. Wang).

E-mail addresses: [jinxq@cqu.edu.cn](mailto:jinxq@cqu.edu.cn) (X. Jin), [qwang@northwestern.edu](mailto:qwang@northwestern.edu) (Q. Wang).

et al., 2005). However, this approach requires a considerable analytical effort due to the difficulty in finding complex potentials that match the interface conditions (Kushch et al., 2005). The well-known equivalent inclusion method (EIM) was proposed by Eshelby (1957, 1959) to treat the elliptical inhomogeneity problem in an infinite medium subjected to uniform loading. The EIM can be effective in handling degenerated 2D plane inhomogeneities, as demonstrated in our recent work (Jin et al., 2014); it is more employed to solve three-dimensional (3D) problems involving a single inhomogeneity (Yu and Kuang, 2003), double inhomogeneities (Moschovidis and Mura, 1975) and even multiple ones (Shodja and Roumi, 2005). The EIM has also been extended to the cases of non-ellipsoidal shapes of inhomogeneities, such as cylinders (Wu and Du, 1995a,b) and arbitrary shapes (Zhou et al., 2011b). In addition to the analytical methods above, the finite element method (FEM) is also widely used (Meguid and Zhu, 1995; Singh et al., 2011) for solving this type of problems. However, due to the requirements for accurate boundary condition descriptions and the long computation time involved, the FEM is not regarded as an efficient way to analyze problems involving infinite dimensions (Zhou et al., 2012).

Several recent publications introduced numerical approaches (Jin et al., 2009; Leroux and Nélías, 2011; Wang et al., 2012b; Zhou et al., 2011a) for problems involving inhomogeneities within a semi-infinite medium based on the EIM through replacing the

inhomogeneities by equivalent inclusions with properly chosen eigenstrains distributed within each inclusion. The eigenstrain is the generic name, defined by Mura (1993), given to such non-elastic strains as thermal expansions, plastic strains, and others. The cuboidal inclusion solution introduced by Chiu (1977) is often utilized as the basis for the numerical methods for determining the equivalent eigenstrains. The eigenstrain within each elementary cuboidal inclusion is considered uniform. The EIM utilized in these methods can thus be viewed as a numerical EIM. The disturbed elastic fields due to the eigenstrains can be formulated in terms of the Galerkin vectors (Liu et al., 2012) or solved based on the method by Zhou et al. (2009).

The present study considers the contact of a sphere and an inhomogeneous half space, and focuses on the influence of distributed non-interpenetrating inhomogeneities on the contact responses of such inhomogeneous materials. Ellipsoidal inhomogeneities are modeled because they can conveniently represent various shapes, such as spheres, flat cracks, and cylindrical microwires. The eigenstrain within each single equivalent ellipsoidal inclusion is assumed uniform for solution efficiency. The proposed new method has two portions: a numerical EIM to determine the eigenstrains together with a superposition scheme, and the solution of the elastic field caused by the eigenstrains using the new analytical solutions (Liu et al., 2012) based on the Galerkin vectors.

## 2. Description of the model and the solution methods

### 2.1. Model description

Suppose that a subdomain  $\Omega$  is embedded in and perfectly bonded within an elastic matrix occupying a half-space. The elastic modulus of the matrix is  $C_{ijkl}$  while that of the subdomain  $\Omega$  is  $C_{ijkl}^*$ . If  $C_{ijkl} \neq C_{ijkl}^*$  is satisfied, the subdomain  $\Omega$  becomes an inhomogeneity. When the matrix experiences an external load, the inhomogeneity should lead to a disturbance in a localized region. Fig. 1 shows the parametric model for a single inhomogeneity in the half-space. Parameters  $x$ ,  $y$  and  $z$  are used to determine the location of the inhomogeneity, whose size is controlled by  $a$ ,  $b$  and  $c$ . The objective of the current work is to investigate the effect of inhomogeneities under the action of a contact pressure, instead of to solve a contact problem (Li et al., 2013; Wang et al., 2012a,b, 2013a). Therefore, the present work will start with a known Hertz

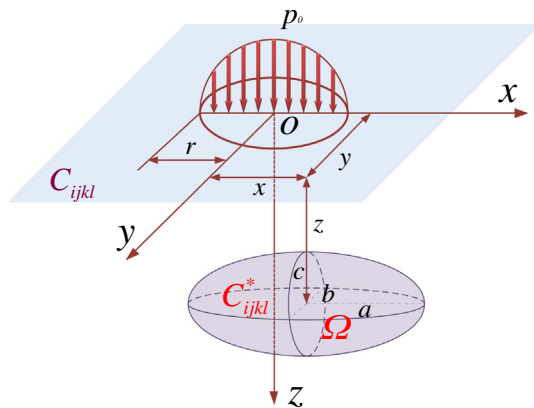


**Fig. 1.** Parametric model for an inhomogeneity in a homogeneous half-space subjected to a Hertz contact load (contact radius  $r$  and maximum pressure  $p_0$ ). Parameters  $x$ ,  $y$ ,  $z$  and  $a$ ,  $b$ ,  $c$  are introduced to determine the location and size of the inhomogeneity.

pressure. A circular Hertz load is applied on the contact area defined by radius  $r$ , and the maximum pressure  $p_0$ . For any point  $s(\alpha, \beta)$  on the surface, the applied normal stress,  $p = p_0 \sqrt{r^2 - \alpha^2 - \beta^2} / r$ .

The basic principle of the EIM is to assume that the existence of an inhomogeneity adds a disturbance to the elastic field of an otherwise homogeneous material. The disturbance can be simulated by the elastic field resulting from a corresponding homogeneous inclusion with appropriately selected eigenstrains. Stress  $\sigma_{ij}$  of any point inside the inhomogeneity shown in Fig. 1 can be solved from the following equation.

$$\sigma_{ij} = C_{ijkl}^* (\varepsilon_{kl}^h + \varepsilon_{kl}) \quad (1)$$

where  $\varepsilon_{kl}^h$  is the strain caused by the Hertzian contact pressure, and  $\varepsilon_{kl}$  is the strain disturbance induced by the inhomogeneity.

The stress  $\sigma_{ij}^h$  induced by the Hertzian contact pressure in the absence of the inhomogeneity is

$$\sigma_{ij}^h = C_{ijkl} \varepsilon_{kl}^h \quad (2)$$

In the equivalent inclusion, the strain,  $\varepsilon_{ij}$ , consists of the elastic strain  $\varepsilon_{ij}$  and eigenstrain  $\varepsilon_{ij}^*$ . The stress disturbance  $\sigma_{ij}$  caused by the inclusion is related to the elastic strain  $\varepsilon_{ij}$  by Hooke's law.

$$\sigma_{ij} = C_{ijkl} \varepsilon_{kl} = C_{ijkl} (\varepsilon_{kl} - \varepsilon_{kl}^*) \quad (3)$$

Note that  $\varepsilon_{ij}$  in the above Eq. (3) is related to the eigenstrain,  $\varepsilon_{ij}^*$ , through the Eshelby tensor  $S_{ijkl}$ .

$$\varepsilon_{ij} = S_{ijkl} \varepsilon_{kl}^* \quad (4)$$

For an infinite space problem, the Eshelby tensor  $S_{ijkl}$  can be expressed as

$$S_{ijkl} = -\frac{1}{2} \int_{-\infty}^{+\infty} C_{mnkl} [G_{im,nj}(x-x') + G_{jm,ni}(x-x')] dx' \quad (5)$$

where  $G_{ij}(x-x')$  is the Green's function, which is also called the fundamental solution, and  $G_{ij,k}(x-x') = \partial/\partial x_k G_{ij}(x-x') = -\partial/\partial x'_k G_{ij}(x-x')$ . The detailed expressions of  $G_{ij}(x-x')$  can be found in the work of Mura (1993). The present work considers the half-space inclusions, and the corresponding Eshelby tensor can be obtained by adding to the full-space solution a compensation term, which will be discussed in details later (cf. Fig. 2).

The EIM principle implies that the superposition of the stresses in Eqs. (2) and (3) is equivalent to the actual stress fields of the inhomogeneity problem (Fig. 1). Substituting Eqs. (2) and (3) to Eq. (1) yields

$$C_{ijkl} (\varepsilon_{kl}^h + S_{klmn} \varepsilon_{mn}^* - \varepsilon_{kl}^*) = C_{ijkl}^* (\varepsilon_{kl}^h + S_{klmn} \varepsilon_{mn}^*) \quad \text{in } \Omega \quad (6)$$

Eq. (6) is the governing equation for implementing the EIM, with which  $\varepsilon_{kl}^*$  can be determined for a single equivalent inclusion. This equation is the core to handle multiple-inhomogeneity cases. Assuming  $n$  non-interpenetrating inhomogeneities arbitrarily distributed in a half space, the strain  $\varepsilon_{ij}(j)$  in the  $j$ th equivalent inclusion is the summation of contributions from all the inclusions within the computational domain, i.e.,

$$\begin{aligned} \varepsilon_{ij}(j) &= S_{ijkl}(1,j) \varepsilon_{kl}^*(1) + \cdots + S_{ijkl}(i,j) \varepsilon_{kl}^*(i) + \cdots + S_{ijkl}(n,j) \varepsilon_{kl}^*(n) \\ &= \sum_{i=1}^n S_{ijkl}(i,j) \varepsilon_{kl}^*(i) \end{aligned} \quad (7)$$

where  $S_{ijkl}(i,j)$  is the Eshelby tensor relating the eigenstrain of equivalent inclusion  $i$  to the corresponding induced strain field of

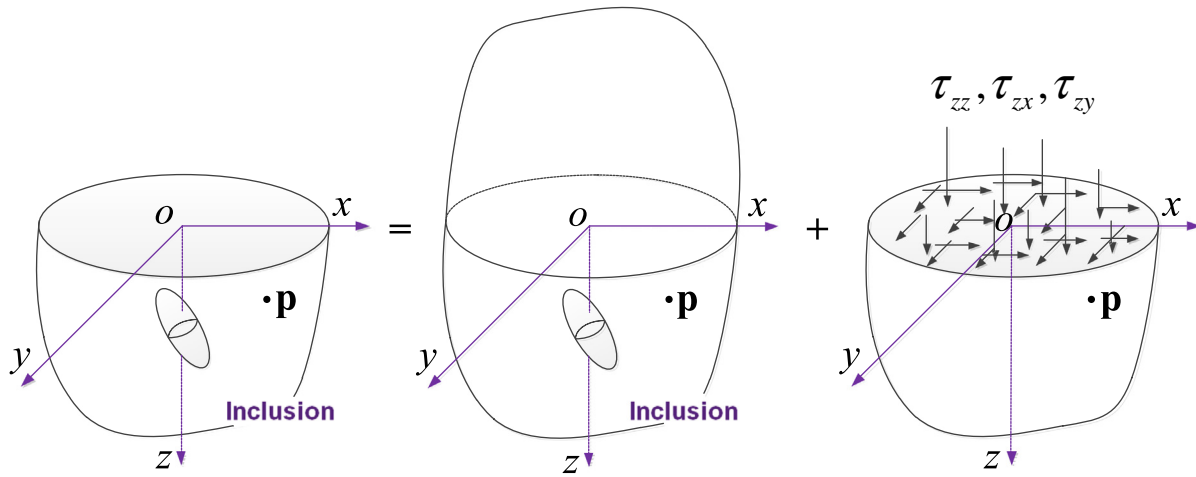


Fig. 2. Schematic of the half-space inclusion solution composed of two parts: the inclusion solution in the full space and the homogeneous solution in the half space with surface traction cancellation.

inclusion  $j$ . Substituting Eq. (7) into Eq. (6) yields following matrix form.

$$\mathbf{A} \boldsymbol{\varepsilon}^* = \mathbf{b}$$

$$\mathbf{A} = \begin{bmatrix} \mathbf{a}(1,1) & \mathbf{a}(1,2) & \cdots & \mathbf{a}(1,j) & \cdots & \mathbf{a}(1,n) \\ \mathbf{a}(2,1) & \mathbf{a}(2,2) & \cdots & \mathbf{a}(2,j) & \cdots & \mathbf{a}(2,n) \\ \vdots & \vdots & \ddots & \vdots & \ddots & \vdots \\ \mathbf{a}(i,1) & \mathbf{a}(i,2) & \cdots & \mathbf{a}(i,j) & \cdots & \mathbf{a}(i,n) \\ \vdots & \vdots & \ddots & \vdots & \ddots & \vdots \\ \mathbf{a}(n,1) & \mathbf{a}(n,2) & \cdots & \mathbf{a}(n,j) & \cdots & \mathbf{a}(n,n) \end{bmatrix}; \quad (8)$$

$$\boldsymbol{\varepsilon}^* = \begin{bmatrix} \boldsymbol{\varepsilon}^*(1) \\ \boldsymbol{\varepsilon}^*(2) \\ \vdots \\ \boldsymbol{\varepsilon}^*(i) \\ \vdots \\ \boldsymbol{\varepsilon}^*(n) \end{bmatrix}; \quad \mathbf{b} = \begin{bmatrix} \mathbf{b}(1) \\ \mathbf{b}(2) \\ \vdots \\ \mathbf{b}(j) \\ \vdots \\ \mathbf{b}(n) \end{bmatrix}$$

where  $\mathbf{a}(i,j) = \mathbf{T}(i,j) - \mathbf{C}^{(j)} \cdot \mathbf{S}(i,j)$ . If  $i=j$ ,  $\mathbf{T}(i,j) = \mathbf{C} \cdot \mathbf{S}(i,j)$ ; if not,  $\mathbf{T}(i,j) = \mathbf{C} \cdot (\mathbf{S}(i,j) - \mathbf{I})$ .  $\mathbf{I}$  is a unit matrix, and  $\mathbf{b}(j) = \mathbf{C}^{(j)} \cdot \boldsymbol{\varepsilon}^0(j) - \boldsymbol{\sigma}^0(j)$ .

Interactions among all inhomogeneities are accounted in Eq. (8). Due to linearity and the randomness of inhomogeneity locations, LU decomposition (Bartels and Golub, 1969) is employed to determine the unknown eigenstrains in Eq. (8).

The current formulation for solving contact problems utilizing the numerical EIM assumes that the eigenstrain in an inclusion in the half-infinite matrix is uniform. Taking the advantage of our new effective superposition approach (Wang et al., 2013b), the stress solution of any point  $\mathbf{p}$  within the matrix is composed of two parts (Fig. 2) instead of three parts presented in the work of Chiu (1977), the inclusion solution in the full space and the homogeneous solution in the half space with surface traction cancellation.

The elastic solutions of the first part for both the interior and exterior points of an inclusion can be solved based on the work of Ju and Sun (1999) and Jin et al. (2011), which provided the closed-form solution of the Eshelby tensor of an ellipsoidal inclusion in an infinite matrix. The Eshelby tensor  $S_{ijkl}$  for an exterior point is expressed as follows.

$$S_{ijkl} = \delta_{ij}\delta_{kl} \left[ \frac{\nu}{1-\nu} G_I^{(1)}(\lambda) + G_{IK}^{(2)}(\lambda) \right] + (\delta_{ik}\delta_{jl} + \delta_{il}\delta_{jk})$$

$$\times \left[ \frac{G_I^{(1)}(\lambda) + G_J^{(1)}(\lambda)}{2} + G_{JJ}^{(2)}(\lambda) \right] + G_I^{(3)}(\lambda)(\delta_{ij}n_k n_l + \delta_{il}n_j n_k)$$

$$+ G_J^{(3)}(\lambda)(\delta_{jk}n_i n_l + \delta_{jl}n_i n_k) + G_K^{(3)}(\lambda)(\delta_{kl}n_i n_j + \delta_{ki}n_j n_l)$$

$$+ G_{ijkl}^{(4)}(\lambda) + [G_{ijkl}^{(5)}(\lambda) + G^{(6)}(\lambda)]n_i n_j n_k n_l \quad (9)$$

where  $\delta_{ij}$  is Kronecker's delta,  $\lambda$  is the largest positive root of Eq. (10) for any point  $\mathbf{p} = (x, y, z)$  located outside of the inclusion.

$$\frac{x^2}{a^2 + \lambda} + \frac{y^2}{b^2 + \lambda} + \frac{z^2}{c^2 + \lambda} = 1 \quad (10)$$

Variable  $n$  in Eq. (9) is the component of the outward unit normal vector  $\mathbf{n} = (n_x, n_y, n_z)$  at point  $\mathbf{p}$  on the imaginary ellipsoidal surface. Detailed expressions of  $G$  are given in Appendix A. The Eshelby tensor,  $S_{ijkl}$ , for the interior field of the inclusion is less complex and can be derived from Eq. (9) by letting  $\lambda$  and  $\mathbf{n}$  vanish (Jin et al., 2011).

On the other hand, the latter part in Fig. 2 is a homogenous solution of the half space with the surface tractions cancellation. In order to solve the subsurface stress field, the corresponding surface tractions domain is decomposed into  $N_x \times N_y$  rectangular elements of the same size. The domain of surface tractions is always two times the domain that encloses all the inclusions considered in the computations in both the  $x$  and  $y$  directions in order to account the traction effect accurately. The stresses at any point  $p(x, y, z)$  in the half space can be expressed as the superposition of contributions from tractions of each surface element  $s(\alpha', \beta')$  as follows (Liu and Wang, 2002).

$$\sigma_{ij}^h(x, y, z) = \sum_{\beta'}^{N_y} \sum_{\alpha'}^{N_x} T_{ij}^S(x - \alpha', y - \beta', z) S(\alpha', \beta')$$

$$+ \sum_{\beta'}^{N_y} \sum_{\alpha'}^{N_x} T_{ij}^P(x - \alpha', y - \beta', z) P(\alpha', \beta') \quad (11)$$

where  $P(\alpha', \beta')$  and  $S(\alpha', \beta')$  are surface tractions,  $T_{ij}^P$  and  $T_{ij}^S$  are the influence coefficients determined by integrating the product of the Green's function and the shape function over each discrete element. Detailed expressions of  $T_{ij}^P$  and  $T_{ij}^S$  are available in Liu and Wang (2002).

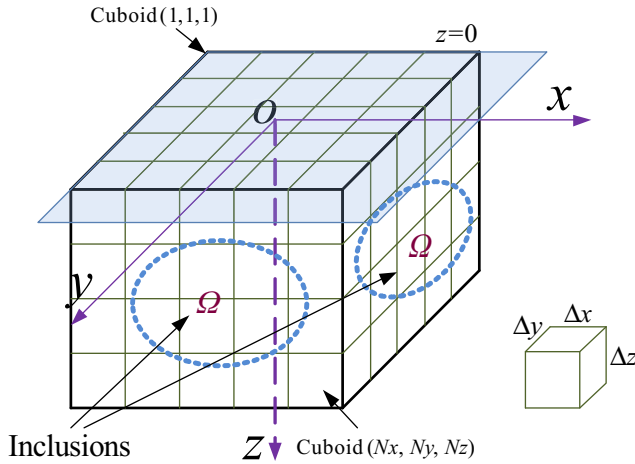


Fig. 3. Discretization for computation.

Table 1

Computation times for different methods using different mesh sizes. (100 arbitrarily distributed inhomogeneities of radius = 0.148r).

Mesh size	The current method (s)	The method by Liu et al. (s)	FEM
16 × 16 × 16	0.8	8.5	2.1 s
32 × 32 × 32	6.1	72.4	25.5 s
64 × 64 × 64	54.3	598.0	1493.3 s
128 × 128 × 128	741.3	7731.1	N.A.

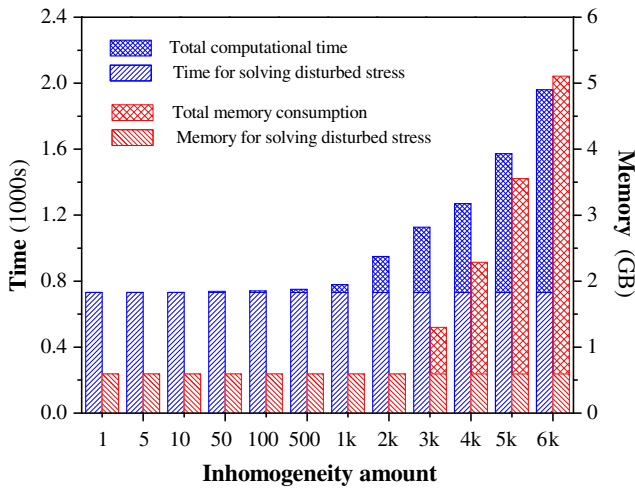


Fig. 4. Computation time and memory usage by the current new method for different numbers of inhomogeneities in a fixed computational domain discretized to 128 × 128 × 128 meshes. (100 arbitrarily distributed inhomogeneities of radius = 0.148r).

## 2.2. Disturbed stress field

The disturbed stress field induced by the eigenstrains is formulated as follows (Liu et al., 2012; Wang et al., 2012b).

$$\begin{aligned}\sigma_{ij}^{out} &= \frac{-\mu}{4\pi(1-\nu)} \int_{\Omega} (\Theta_{ij} - \bar{\mathbf{R}}_{ij}^l - \bar{\mathbf{R}}_{ij} - 2z\bar{\mathbf{R}}_{3ij} + 2z^2\bar{\Phi}_{ij}) [\mathbf{e}^*] d\mathbf{s} \sigma_{ij}^{in} \\ &= \sigma_{ij}^{out} - 2\mu e_{ij}^* - \frac{2\mu}{1-\nu} \nu e_{kk}^* \delta_{ij}\end{aligned}\quad (12)$$

where  $\sigma_{ij}^{out}$  and  $\sigma_{ij}^{in}$  are the stress disturbances of points located outside of and inside  $\Omega$ , respectively, and  $[\mathbf{e}^*] = [e_{11}^*, e_{22}^*, e_{33}^*, 2e_{23}^*, 2e_{13}^*, 2e_{12}^*]$ . Vector  $\mathbf{s}$  indicates a source or excitation point. Vec-

tors  $\Theta$ ,  $\bar{\mathbf{R}}^l$ ,  $\bar{\mathbf{R}}$  and  $\bar{\Phi}$  are the second-order derivatives of the potentials. Double bars denote double derivatives, and the comma sign associated with each of them indicates partial differentiation. These vectors are utilized for further simplification of the expressions for the disturbed elastic field, and

$$\begin{aligned}\bar{\mathbf{R}} &= [R_{11} \ R_{22} \ R_{33} \ -R_{23} \ -R_{13} \ R_{12}] \\ \bar{\mathbf{R}}^l &= [R_{11}^l \ R_{22}^l \ R_{33}^l \ R_{23}^l \ R_{13}^l \ R_{12}^l] \\ \bar{\Phi} &= [\phi_{11} \ \phi_{22} \ \phi_{33} \ -\phi_{23} \ -\phi_{13} \ \phi_{12}] \\ \Theta &= [\Theta_{11} \ \Theta_{22} \ \Theta_{33} \ \Theta_{23} \ \Theta_{13} \ \Theta_{12}]\end{aligned}\quad (13)$$

Assume that  $(\alpha, \beta, \gamma)$  denotes a response point, while  $(\alpha', \beta', \gamma')$  is a source or excitation point, then

$R^l = \sqrt{(\alpha - \alpha')^2 + (\beta - \beta')^2 + (\gamma - \gamma')^2}$ ,  $R = \sqrt{(\alpha - \alpha')^2 + (\beta - \beta')^2 + (\gamma + \gamma')^2}$ , and  $\phi = 1/R$ .  $R^l$  and  $R$  are bi-harmonic potentials and  $\phi$  is a kind of harmonic potentials.  $\Theta$  is defined in detail in the work of Liu et al. (2012).

The domain for calculation is discretized into finite cuboidal elements ( $N_x \times N_y \times N_z$ ) of the same size (Fig. 3). Each cuboid has three sides of length  $\Delta x$ ,  $\Delta y$ ,  $\Delta z$  in the  $x$ ,  $y$ , and  $z$  directions, respectively. The eigenstrain,  $e_{kl}^*$ , inside each of the elements is approximately uniform, where the elastic field is obtained by summation of contributions from all the elements using  $K_{ijkl}^{(0)}$ ,  $K_{ijkl}^{(1)}$ ,  $K_{ijkl}^{(2)}$  and  $K_{ijkl}^{(3)}$ , the influence coefficients relating the eigenstrains with the disturbed stresses.

$$\begin{aligned}\sigma_{ij}(\alpha, \beta, \gamma) &= \frac{\mu}{4\pi(1-\nu)} \left( \sum_{\gamma'=1}^{N_z} \sum_{\beta'=1}^{N_y} \sum_{\alpha'=1}^{N_x} K_{ijkl}^{(0)} (\alpha - \alpha', \beta - \beta', \gamma - \gamma') e_{kl}^*(\alpha', \beta', \gamma') \right. \\ &\quad + \sum_{\gamma'=1}^{N_z} \sum_{\beta'=1}^{N_y} \sum_{\alpha'=1}^{N_x} K_{ijkl}^{(1)} (\alpha - \alpha', \beta - \beta', \gamma + \gamma') e_{kl}^*(\alpha', \beta', \gamma') \\ &\quad + \gamma \sum_{\gamma'=1}^{N_z} \sum_{\beta'=1}^{N_y} \sum_{\alpha'=1}^{N_x} K_{ijkl}^{(2)} (\alpha - \alpha', \beta - \beta', \gamma + \gamma') e_{kl}^*(\alpha', \beta', \gamma') \\ &\quad \left. + \gamma^2 \sum_{\gamma'=1}^{N_z} \sum_{\beta'=1}^{N_y} \sum_{\alpha'=1}^{N_x} K_{ijkl}^{(3)} (\alpha - \alpha', \beta - \beta', \gamma + \gamma') e_{kl}^*(\alpha', \beta', \gamma') \right),\end{aligned}\quad (14)$$

$(1 \leq \alpha \leq N_x, 1 \leq \beta \leq N_y, 1 \leq \gamma \leq N_z)$

The four multi-level summations on the right hand side of Eq. (14) are related to discrete convolution and correlation. Here, the first term can be calculated using the 3D discrete convolution and FFT (DC-FFT) algorithm (Liu and Wang, 2002; Liu et al., 2000), while the other three terms can be efficiently handled through the combined 3D discrete convolution-discrete correlation and FFT (DC-DCR-FFT) algorithm (Liu and Wang, 2005). The current work has demonstrated that those FFT-related algorithms can significantly reduce the computational burden.

Take the influence coefficient,  $K_{ijkl}^{(2)}$ , in one of the convolution-correlation terms as an example, the detailed expressions of the influence coefficients can be determined as follows.

$$\begin{aligned}K_{ijkl}^{(2)}(\alpha - \alpha', \beta - \beta', \gamma + \gamma') &= -k_{ijkl}(x_1, y_1, z_1) + k_{ijkl}(x_2, y_1, z_1) \\ &\quad - k_{ijkl}(x_2, y_2, z_1) + k_{ijkl}(x_1, y_2, z_1) \\ &\quad - k_{ijkl}(x_1, y_2, z_2) + k_{ijkl}(x_1, y_1, z_2) \\ &\quad - k_{ijkl}(x_2, y_1, z_2) + k_{ijkl}(x_2, y_2, z_2)\end{aligned}\quad (15)$$

where

$$\begin{aligned}x_1 &= \alpha - \alpha' - \Delta x/2; & x_2 &= \alpha - \alpha' + \Delta x/2; \\ y_1 &= \beta - \beta' - \Delta y/2; & y_2 &= \beta - \beta' + \Delta y/2; \\ z_1 &= \gamma - \gamma' - \Delta z/2; & z_2 &= \gamma - \gamma' + \Delta z/2.\end{aligned}\quad (16)$$

Details for functions  $k_{ijkl}(\xi_1, \xi_2, \xi_3)$  in Eq. (15) are given in Appendix A2 in the paper of Liu et al. (2012). For instance,  $k_{1113}(\xi_1, \xi_2, \xi_3)$  can be derived as following.

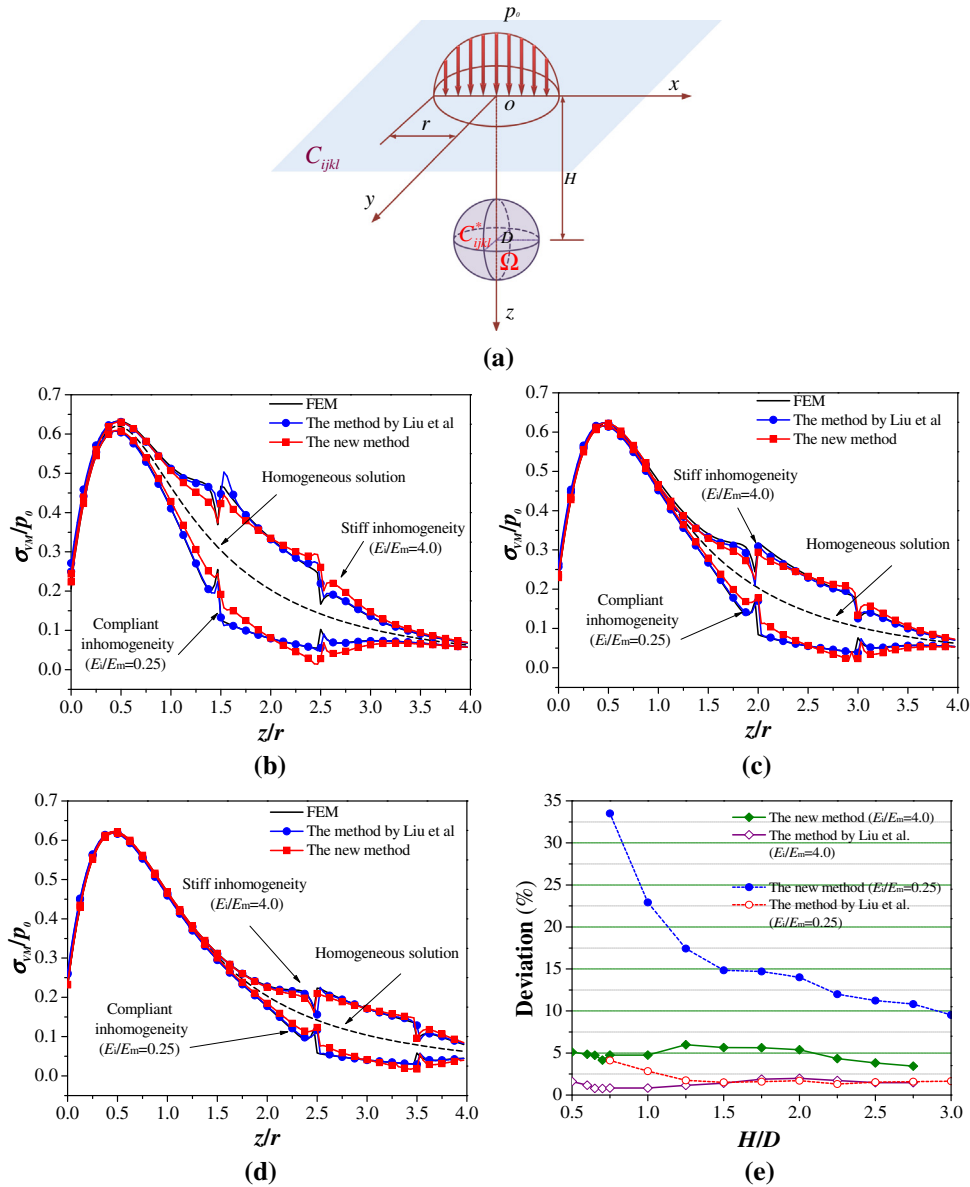


**Fig. 5.** Comparison for accuracy evaluation. (a) A spherical inhomogeneity for result comparison; (b) von Mises stress distributions along the  $z$ -direction obtained by the three methods,  $H/D = 2.0$ ; (c) von Mises stress distributions along the  $z$ -direction obtained by the three methods,  $H/D = 2.5$ ; (d) von Mises stress distributions along the  $z$ -direction obtained by the three methods,  $H/D = 3.0$ ; (e) average relative deviations of the stress solved by the numerical methods. FEM solutions from a finer mesh are used as references.

$$k_{1113}(\xi_1, \xi_2, \xi_3) = -4HA_{1,111}(\xi_1, \xi_2, \xi_3) + 4vA_{1,133}(\xi_1, \xi_2, \xi_3) + 2A_{2,13311}(\xi_1, \xi_2, \xi_3) \quad (17)$$

where  $H = 1 - \nu$ ,  $A_i$  ( $i = 0, 1, 2, 3$ ) is the integral forms for the mentioned bi-harmonic potentials and harmonic potentials; while their detailed expressions can be found in Eqs. (23)–(26) in the paper of Liu et al. (2012). Moreover, the explicit expressions of the influence coefficient,  $K_{ijkl}^{(0)}$ , in the convolution term of Eq. (14) are listed in Appendix A in one of our recent works (Wang et al., 2013b).

### 3. Model validation and results verification

Comparative analyses are performed to evaluate the efficiency and accuracy of the new method. The results obtained are compared with those solved by the FEM and the accurate numerical method of Liu et al. (2012), which is based on the numerical EIM and Galerkin vectors. Note that the conjugate gradient method

(CGM) (Polonsky and Keer, 1999) combined with the 3D-FFT (Zhou et al., 2011a) are applied to solve for the unknown eigenstrains in Liu et al. (2012).

#### 3.1. Efficiency, memory usage and accuracy

Table 1 compares the calculation efficiency of the proposed and reference methods for solving the problem involving 100 arbitrarily distributed spherical inhomogeneities. The volume fraction of the inhomogeneity is about 5%; the computational domain of  $3r \times 3r \times 3r$  ( $r$  is the contact radius) is discretized with different meshes, and the radius of the inhomogeneities is  $0.148r$ . All computations are performed on a personal computer with a 2.60 GHz i7 quad-core CPU and 8.0 GB memory. The table reveals that with the same discretization, the computation time used by the new method is much shorter than that by the other two methods.



The computation time and memory consumption for the FEM increase sharply with mesh size. The computation time used for the LU decomposition and the proposed method increases with the number of unknowns. Fig. 4 shows the time and memory used by the new method with the  $128 \times 128 \times 128$  discretization of the same computational domain. The number of arbitrarily distributed spherical inhomogeneities changes from 1 to 6000. The radius of the inhomogeneities is set to be  $0.02r$ ; the volume fraction of the inhomogeneities changes with the variation of the amount of inhomogeneities. The time consumption and memory occupation for determining the disturbed stress field depend only on the discretization. With a fixed discretization, the computation time and memory usage remain the same, 731 s and 595 MB, respectively (Fig. 4). The two values are the same as those when using the accurate numerical method of Liu et al. (2012) for solving the disturbed stress field because of the same basis of the Galerkin vectors.

The total computation time and memory usage required by the method of Liu et al. (2012) are determined by the mesh size only if the iterative number is fixed. However, the efficiency of the new method is advantageous in eigenstrain determination, mainly due to the fact that ellipsoidal inhomogeneities, rather than rectangular elements generated by discretization, are employed as the basic element. Assuming there are  $n$  inhomogeneities in the computational domain discretized with  $N_x \times N_y \times N_z$  meshes. The computational time for the current method in determining the unknown eigenstrains within the inclusions is  $O(2n^3/3)$ , while for existing methods, like the method by Liu et al. (2012), the corresponding time for one iteration is  $3456N_xN_yN_z \ln 8N_xN_yN_z$  (Wang et al., 2013b). The inhomogeneity number is always far less than that of the mesh, therefore, the current method can increase the computational efficiency. A considerable memory size would be consumed by the new method if the number of inhomogeneities becomes significantly larger due to the LU decomposition, which could be a possible constraint for the application of the new method in solving the contact problems of inhomogeneous materials with densely distributed inhomogeneities.

### 3.2. Accuracy

A single spherical inhomogeneity problem (Fig. 5a) is solved for accuracy evaluation. Set the diameter of the inhomogeneity as  $D = r$ . The depth,  $H$ , is defined as the distance from the center of the inhomogeneity to the surface. The computational domain is selected to be  $4r \times 4r \times 4r$  ( $r$  is the contact radius) and the mesh of  $128 \times 128 \times 128$  is used to discretize the computational domain. The results by the FEM with a finer discretization are employed as references. Both stiff ( $E_i/E_m = 4.0$ ) and compliant ( $E_i/E_m = 0.25$ ) inhomogeneities are considered. The Young's moduli of the inhomogeneity and matrix are, respectively,  $E_i$  and  $E_m$ .

The von Mises stress fields of the case with  $H/D = 2.0$  computed with the current method, the method by Liu et al. (2012) and the FEM are shown in Fig. 5b. The stress field is disturbed by the inhomogeneities, and the stress is higher inside the stiff inhomogeneity. On the other hand, stress reduction is observed inside the compliant inhomogeneity. Both the current method and the method by Liu et al. (2012) capture the disturbance of the elastic field, but the latter produce more accurate results, especially in the region closer to and within the inhomogeneity. The accuracy of the current method increases when  $H/D$  changes to 2.5 and 3.0, the inhomogeneity moving away from the surface, as shown in Fig. 5c and d. The method by Liu et al. (2012) has advantage in accuracy compared with the present method. The relative inaccuracy of the current method is due to assumption of uniform eigenstrain within each ellipsoidal inclusion in the semi-infinite medium. This is a trade-off for the high computational speed.

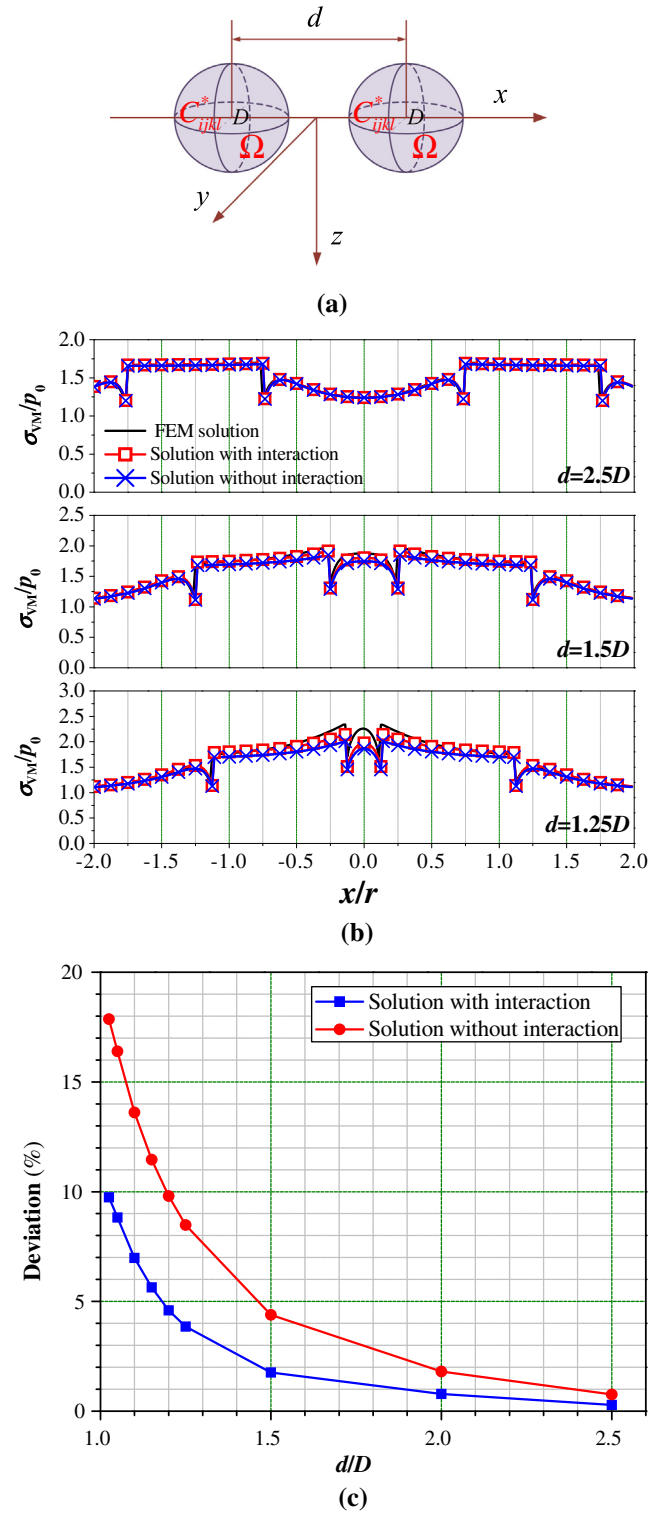


**Fig. 6.** Effect of inhomogeneity distance on the solution accuracy. (a) Double inhomogeneity problem. The double inhomogeneities are embedded in an infinite matrix, subjected to a remote external load  $p_0$  in the  $y$ - $y$  direction. The elastic modulus of inhomogeneities is four times that of the matrix; (b) von Mises stress distributions along the  $x$ -direction solved by the FEM, the current method and the incomplete solution for  $d = 2.5D$  (upper),  $d = 1.5D$  (middle) and  $d = 1.25D$  (lower), respectively; (c) deviations of the numerical results produced by the current method and the incomplete method from the FEM results (solved with a finer mesh) as a function of inhomogeneity distance  $d$ .

More calculations were conducted in order to understand quantitatively the influence of the assumption of the uniform eigenstrain distribution in each inclusion on the solution accuracy. The

same spherical inhomogeneity (Fig. 5a) is used again but its location varies to approach the surface of the semi-infinite matrix. The same discretization,  $128 \times 128 \times 128$ , is applied. In our recent study (Zhou et al., 2014), the stress concentrations for 2D elliptical inhomogeneities have been studied. The deviations of the stress concentration factors obtained by a similar numerical method were proven acceptable for the 2D calculations. In this work, average relative error analyses of the current method against the FEM solutions solved with a much finer mesh are conducted in order to calibrate the current method. The average relative errors of the von Mises stresses along the  $z$ -direction, defined by Eq. (18), are plotted in Fig. 5e.

$$\delta = \sum_{i=1}^N \frac{|\sigma_{vm}^i - \sigma_{vm}^{F,i}|}{|\sigma_{vm}^{F,i}| N} \times 100\% \quad (18)$$

where  $\sigma_{vm}^i$  is the von Mises stress obtained by one of the numerical methods at the  $i$ th element;  $\sigma_{vm}^{F,i}$  is that by the FEM.  $N$  is the total amount of elements considered in the comparison.

As the depth,  $H$ , of the inhomogeneity changes from  $3.0D$  to  $0.5D$ , the result accuracy of the method by Liu et al. (2012) is well maintained while the results from the new method deviate more notably. However, the obtained results also confirm that the proposed method performs better in accuracy when  $H/D$  increases. The comparative study suggests that the use of the proposed new method should avoid the cases with inhomogeneities close to the matrix surface. Specifically, in order to obtain reasonably accurate results with average errors less than 10%, the location depth  $H$  for a compliant inhomogeneity must not be smaller than  $3.0D$  (Fig. 5e).

The accuracy of the new method for solving a multiple-inhomogeneity case is studied next. Double inhomogeneities are considered (Fig. 6a), where the inhomogeneities have same size

and elastic properties ( $E_i/E_m = 4.0$ ). In order to eliminate the influence of the surface when studying the interaction between two inhomogeneities, one may assume that the two inhomogeneities are perfectly embedded in an infinite matrix. Remote external load  $p_0$  is applied in the  $y$ - $y$  direction. The distance between the centers of the two inhomogeneities is  $d$ . The stiff inhomogeneity cases are considered here. Distance  $d$  is varied from  $2.5D$  to  $1.025D$ . Fig. 6b illustrates the von Mises stress distributions solved by the FEM, the new method and the one without considering inhomogeneity interaction (named as the incomplete solution), respectively. The upper part of the figure shows the results of the double-inhomogeneity problem for  $d = 2.5D$ . Both the new method and the incomplete solution can achieve good results as compared with those by the FEM. Thus, when two inhomogeneities are sufficiently far from each other, the interaction between them is negligible. As the two inhomogeneities move closer, their interaction becomes more significant. When distance  $d$  between the inhomogeneities becomes  $1.5D$ , the stress fields within the inhomogeneities become non-uniform. However, in this case, the proposed method still captures the disturbed stress field well. The results of the incomplete solution deviate from the FEM solution. When the distance is reduced to  $1.25D$ , the stresses between the two opposite ends of the inhomogeneities increase sharply. The results from both methods deviate from those solved with the FEM, and the incomplete solution produces worse results.

By changing the distance  $d$ , shown in Fig. 6a, the relative deviations of the von Mises stresses solved by the new method and the incomplete method are shown in Fig. 6c. When the distance between inhomogeneities is larger than  $1.025D$ , the proposed new method can yield relatively accurate results with less than 10% error with respect to the solutions obtained with the FEM while achieving high efficiency in computation.

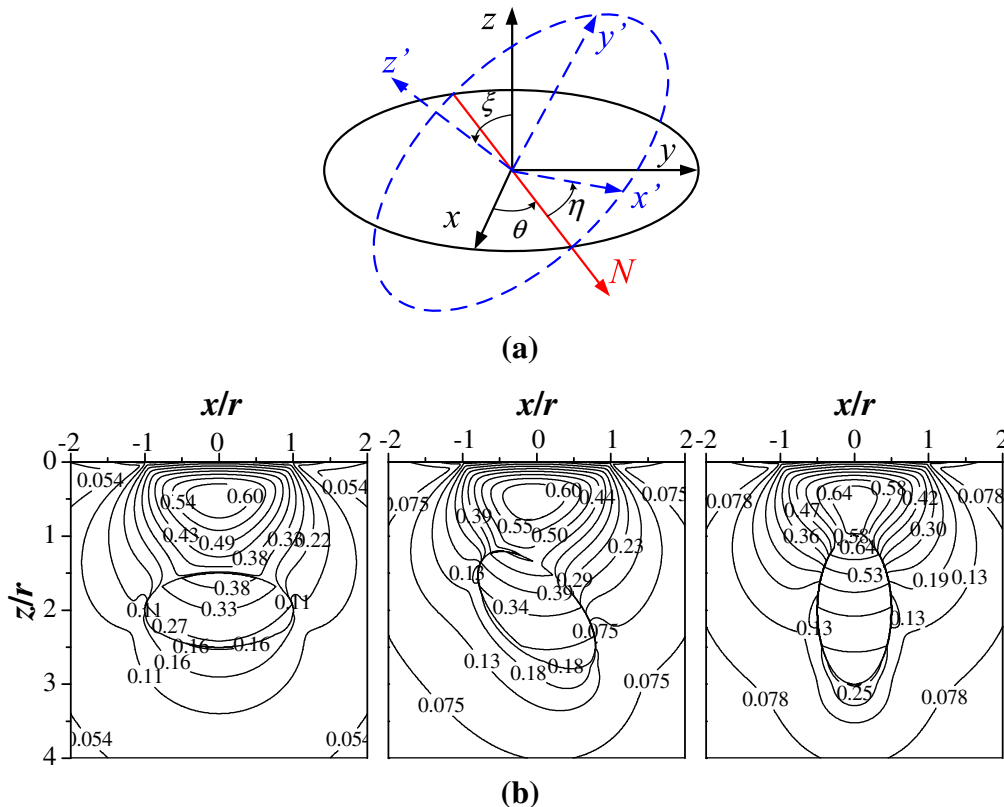
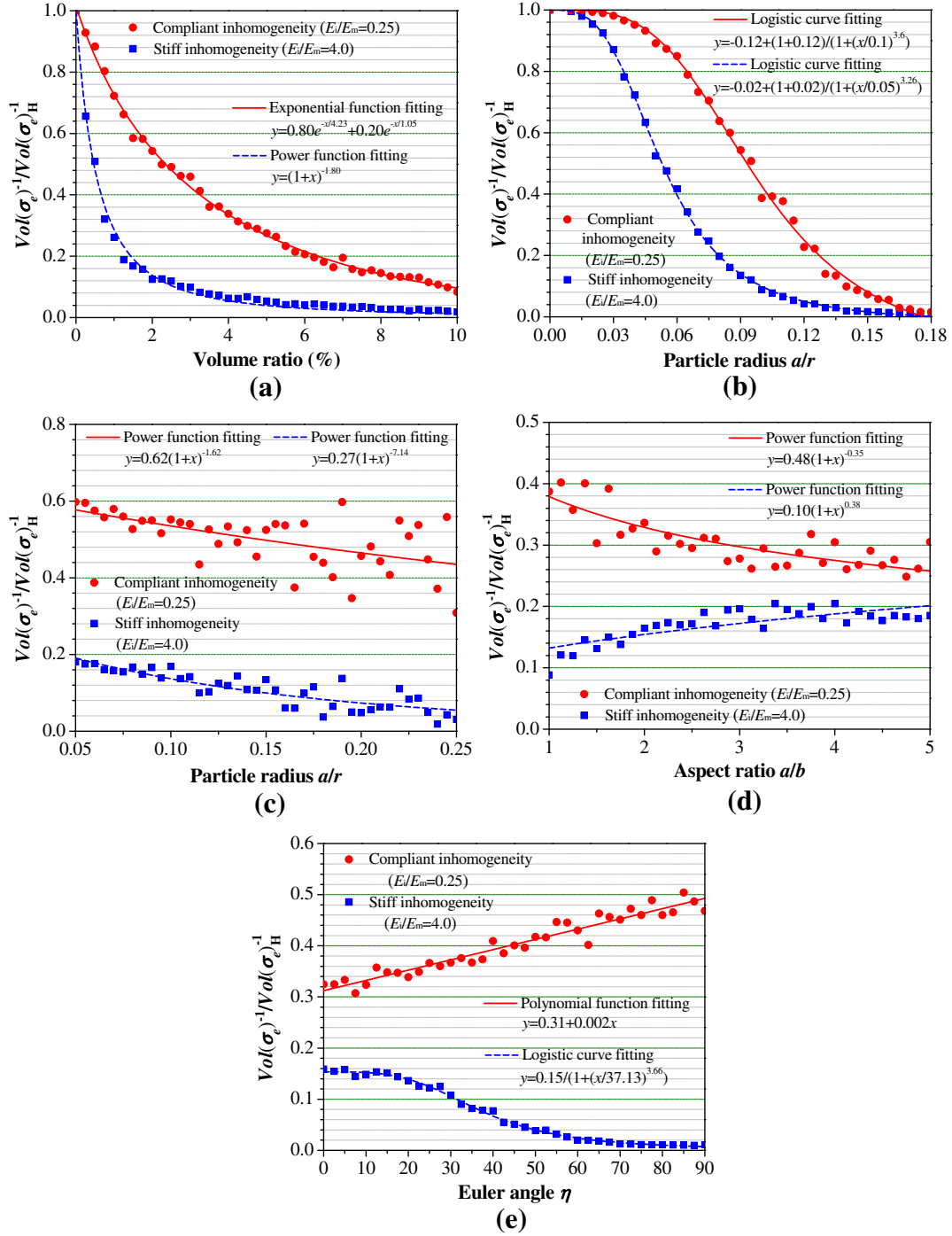


Fig. 7. Effect of inhomogeneity spatial orientation on the contact elastic field of the matrix. (a) Euler angles; (b) von Mises stress distributions disturbed by an inhomogeneity of different orientations.



**Fig. 8.** Variations of the inverse volumetric stress integral as functions of inhomogeneity distribution parameters. (a) Volume ratio; (b) inhomogeneity size at a given number of inhomogeneities; (c) inhomogeneity size at a given volume ratio; (d) aspect ratio; (e) spatial orientation.

#### 4. Applications of the new method

##### 4.1. Inhomogeneity with arbitrary orientation

Spatially distributed inhomogeneities may appear at any arbitrary orientations. In this paper, Euler angles  $\theta$ ,  $\xi$  and  $\eta$  are introduced to characterize the orientations of an inhomogeneity, as shown in Fig. 7a. Using the Euler angles, the rotation matrix,  $\mathbf{A}$ , is defined as (Shabana, 2005)

$$\mathbf{A} = \begin{bmatrix} a_{11} & a_{12} & a_{13} \\ a_{21} & a_{22} & a_{23} \\ a_{31} & a_{32} & a_{33} \end{bmatrix} \quad (19)$$

where

$$\begin{aligned} a_{11} &= \cos \theta \cos \eta - \sin \eta \sin \theta \cos \xi; \\ a_{12} &= \sin \theta \cos \eta + \sin \eta \cos \theta \cos \xi; \\ a_{13} &= \sin \xi \sin \eta; \quad a_{21} = -\cos \theta \sin \eta - \cos \xi \sin \theta \cos \eta; \\ a_{22} &= -\sin \theta \sin \eta + \cos \xi \cos \theta \cos \eta; \quad a_{23} = \sin \xi \cos \eta; \\ a_{31} &= \sin \theta \sin \xi; \quad a_{32} = -\cos \theta \sin \xi; \quad a_{33} = \cos \xi \end{aligned}$$

Any rotation matrix can be decomposed to a product of three elemental rotation matrices, corresponding to the three Euler angles. An ellipsoidal inhomogeneity is used to show the effect of the spatial orientation of the inhomogeneity on the elastic field of the



matrix. The aspect ratio of the model  $t = a/b = a/c = 2.0$ . Set  $\theta = 0^\circ$ ,  $\xi = 90^\circ$  and  $\eta = 0^\circ, 45^\circ$  and  $90^\circ$  respectively. Fig. 7b shows the corresponding von Mises stress fields of the three cases. The present method is also capable of considering the orientation of distributed inhomogeneities, and the detail is given in the next section.

#### 4.2. Parametric study on the volumetric stress integral

Zaretsky (1987) proposed a fatigue life model to predict the fatigue life of rolling bearings. The probability of survival,  $S$ , can be expressed through the volumetric integral of an equivalent stress over the stressed volume,  $\int \int \int_V \sigma_e dV$ , and the contact fatigue life  $N$  as follows using  $e$  as the Weibull slope and  $c$  as the stress exponent.

$$\ln \frac{1}{S} \sim N^e \int \int \int_V \sigma_e^{ec} dV \quad (20)$$

The exponents used in the equation above are material constants to be determined from experimental data. The subsurface stress distribution can be calculated through the proposed new method. The von Mises stress is selected as the equivalent stress in the model. The stress cycle,  $N$ , is almost inversely proportional to the volumetric stress integral  $\int \int \int_V \sigma_e^{ec} dV$  when the failure probability is  $S = 50\%$  (Greco et al., 2010). Thus, the approximate trend of the contact fatigue life of a material with distributed inhomogeneities can be qualitatively characterized. As mentioned

in Section 2.2, the computational domain is discretized into  $N_x \times N_y \times N_z$  cuboidal elements of the same size.  $Vol(\sigma_e)$  is employed to express the volumetric stress integral, i.e.,

$$Vol(\sigma_e) = \sum_{\gamma} \sum_{\beta} \sum_{\alpha} \sigma_e^{ec}(\alpha, \beta, \gamma) \quad (21)$$

In the following, the value of the inverse volumetric stress integral is normalized by that of the homogenous case of the matrix material,  $Vol(\sigma_e)_H$  ( $Vol(\sigma_e)_H = \sum_{\gamma} \sum_{\beta} \sum_{\alpha} \sigma_e^{(h)ec}(\alpha, \beta, \gamma)$ ).  $\sigma_e^{(h)}$  is the obtained equivalent stress for the homogenous case. Both stiff ( $E_i/E_m = 4.0$ ) and compliant ( $E_i/E_m = 0.25$ ) inhomogeneities are considered. The computational domain is selected to be  $3r \times 3r \times 3r$  discretized into  $128 \times 128 \times 128$  meshes. The involved inhomogeneities in the following computations are arbitrarily distributed. A random number generation subroutine in Fortran (Chapman, 2004) is used to determine the locations of the arbitrarily distributed inhomogeneities.

##### 4.2.1. Volume ratio

The influence of the volume ratio of the inhomogeneities on the inverse volumetric stress integral is investigated first. The chosen inhomogeneities are equal-size spheres with the radius  $a$  of  $0.1r$ . The volume ratio varies from 0.0% to 10.0%. It is also ensured that the distance between inhomogeneities is no less than  $2.05a$  for model accuracy. The results are plotted in Fig. 8a. Both stiff and compliant inhomogeneities could cause reductions of the inverse integral, which suggests reductions in the material contact fatigue life. The inverse integral becomes smaller when the value of the

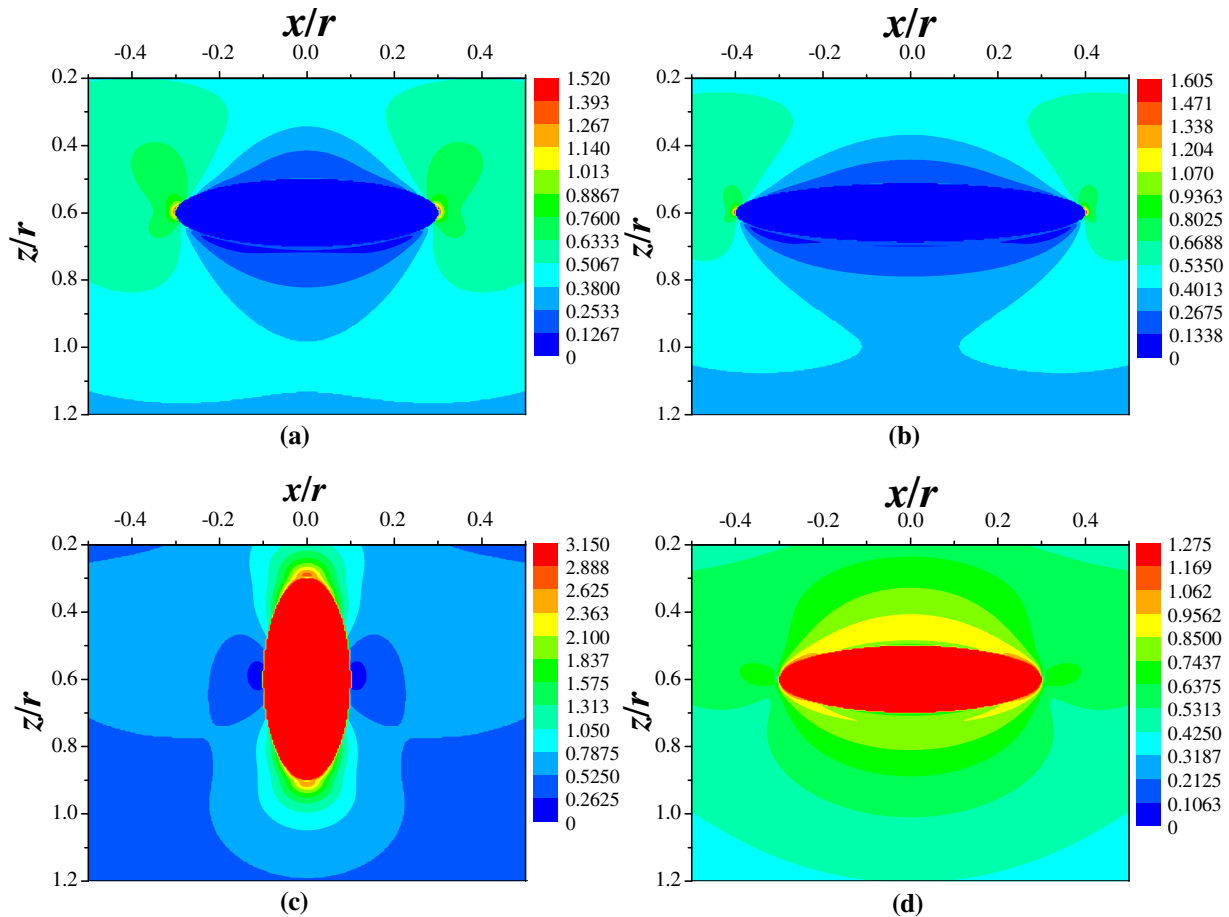


Fig. 9. von Mises stress fields and stress concentrations caused by an inhomogeneity. (a) A cavity with aspect ratio  $t = 3.0$ ; (b) a cavity with aspect ratio  $t = 4.62$ ; (c) a rigid inhomogeneity with aspect ratio  $t = 1/3$ ; (d) a rigid inhomogeneity with aspect ratio  $t = 3.0$ .

volume ratio becomes larger because more inhomogeneities of the same size are embedded in the domain, causing stronger interactions between those inhomogeneities. Moreover, the inverse integral generated by the distributed stiff inhomogeneities is found to be lower than those by the compliant inhomogeneities. As mentioned before, a compliant inhomogeneity may cause reduced stress inside it and in its surrounding when the material mismatch between the two materials is not high. The obtained data well fit to an exponential function and a power function, shown in Fig. 8a, for the compliant and stiff inhomogeneities, respectively.

#### 4.2.2. Inhomogeneity size

The domain including 200 spherical inhomogeneities of the same size, varying from  $0r$  to  $0.18r$ , is analyzed first to study the effect of inhomogeneity size. It is difficult to generate distribution of large size inhomogeneities due to the non-interpenetrating assumption. The simulation results are shown in Fig. 8b. Similar to what observed in the volume fraction effect, higher inverse integral values are found for the compliant inhomogeneities than for the stiff ones. When the inhomogeneities become larger in size, the volume ratio of the inhomogeneity increases as well, and a more severe reduction in the inverse integral value is expected. Next, the volume fraction of spherical inhomogeneities is fixed at 2%. In this case, the radii of the inhomogeneities vary from  $0.05r$  to  $0.25r$ . As shown in Fig. 8c, the downward trends of the integral values for both the stiff and compliant cases become flatter than those in Fig. 8b. This means the volume ratio influences more than size on the integral value.

#### 4.2.3. Aspect ratio

The aspect ratio of 200 inhomogeneities,  $t = a/b = a/c$ , varies from 1.0 to 5.0. The volume fraction of the inhomogeneities is maintained at 3%. Fig. 8d plots the computational results. The effect of the aspect ratio is not as significant as that of the volume ratio. Moreover, the aspect ratio for stiff and compliant inhomogeneities produces contrary effects on the inverse integral. To be specific, the inverse integral slightly increases when the aspect ratio of stiff distributed inhomogeneities continues to increase; the trend reverses for compliant inhomogeneities. The inverse integral is more sensitive to stresses of higher values due to the exponents in Eq. (20), and the difference is related to the stress concentrations of the inhomogeneity. Fig. 9 shows the stress fields and stress concentrations for two extreme cases of inhomogeneities, a cavity and a rigid ellipsoid. When the aspect ratio is larger, the stress concentration is stronger for the former (Fig. 9a and b) at the ends of the major axes. The stress increases within the rigid inhomogeneities, but this effect becomes weaker when the aspect ratio is larger, as shown in Fig. 9c and d.

#### 4.2.4. Spatial orientation

The spatial orientation of a single inhomogeneity causes the variation of the elastic field, and so does that of the 200 inhomogeneities of the same size with the semi major axis  $a = 0.1r$  and the aspect ratio  $t = 2$ . The volume inhomogeneity ratio is 0.77%. Due to the symmetric characteristic of the model, the inhomogeneities only need to be rotated around their minor axis (setting the Euler angles  $\theta = 0^\circ$ ,  $\zeta = 90^\circ$ , while changing  $\eta$  from  $0^\circ$  to  $90^\circ$ ) in the  $y$ -direction. The results are shown in Fig. 8e. If the distributed inhomogeneities are rotated clockwise, the inverse integral increases slightly for the compliant case. As stated above, exterior load causes stress concentrations at the ends of the semi axes perpendicular to the loading direction for the compliant inhomogeneities (Fig. 9a and b). The major axis of the compliant inhomogeneity is perpendicular to the load initially, and the maximum stress concentrations are seen at their vertexes. When the

inhomogeneity is rotated clockwise, the longest axis is no longer parallel to the surface and the stress concentration effect is reduced, leading to the increase in the inverse integral. For stiff inhomogeneities, the same rotation causes the opposite change of the inverse integral.

#### 4.2.5. Elastic modulus

In above parametric studies, the existence of distributed inhomogeneities with the two different moduli produces very different results. Therefore, it is necessary to investigate the effect of modulus variation on the inverse volumetric stress integral of heterogeneous materials. The spherical inhomogeneities with radius  $a = 0.1r$  were analyzed, and two cases with volume ratios of 1% and 3% were taken into consideration. For the stiff inhomogeneity cases, the modulus of the inhomogeneity is normalized by the matrix modulus and the modulus ratio changes from 1 to 40. For the compliant case, the matrix modulus is normalized by that of the inhomogeneity as an independent variable ranging from 1 to 40.

The results are represented in Fig. 10a and b. Again, the cases with the higher volume ratio would generate smaller inverse integrals, consistent with the results of the volume ratio effect mentioned above. For cases with same material mismatch between the matrix and inhomogeneity, the obtained results for the stiff and compliant cases are different. The compliant inhomogeneity groups produce relative higher inverse integral values. In addition, if the mismatch between the two materials is larger, the achieved

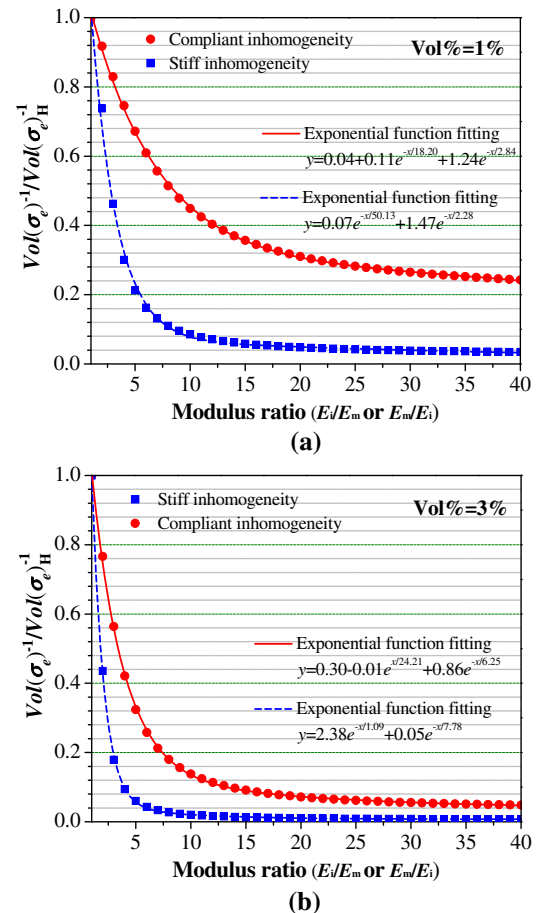


Fig. 10. Variations of the inverse volumetric stress integral as functions of Young's modulus of the inhomogeneities. (a) Volume ratio = 1%; (b) volume ratio = 3%.

integral values become smaller for both the stiff and compliant cases due largely to the local stress increases.

## 5. Conclusions

An efficient approximate numerical method for studying the influence of distributed non-interpenetrating inhomogeneities on the contact properties of inhomogeneous materials is proposed in this paper. The method is based on the equivalent inclusion method, developed using the superposition principle and the disturbed stress field solutions of Liu et al. (2012). Ellipsoidal inhomogeneities are considered as the fundamental elements instead of the cuboid solutions used previous numerical methods. This modification greatly improves the computation efficiency as long as the distance between inhomogeneities,  $d$ , is large than  $1.025D$  for an error smaller than 10%. Inhomogeneity distribution parameters of stiff and compliant inhomogeneities were investigated for their effects on the inverse volumetric stress integral, and corresponding curve fitting equations were obtained. The following conclusions are obtained.

- (1) Decrease in the inverse integral caused by stiff inhomogeneities is always more severe than that by compliant inhomogeneities.
- (2) Increase in inhomogeneity volume ratio, particle size, and material mismatch cause the inverse integral to decrease for both the stiff and compliant cases.
- (3) Inhomogeneities with higher aspect ratios induce a reduction in the inverse integral for the cases of compliant inhomogeneities and an increase in the inverse integral for the stiff cases.
- (4) A larger Euler angle  $\eta$  leads to an increase in the inverse integral for the cases with compliant inhomogeneities and a decrease of the inverse integral for the cases with stiff inhomogeneities.

## Acknowledgments

The authors would like to acknowledge the supports from Center for Surface Engineering and Tribology at Northwestern University, USA, and State Key Laboratory of Mechanical Transmission at Chongqing University (No. 0301002109162), China. The authors are grateful to Prof. Wenzhong Wang for valuable discussions. Qinghua Zhou would like to thank the scholarship support from China Scholarship Council (No. 2011605076). Zhanjiang Wang would also like to acknowledge the support from National Science Foundation of China under Grant No. 51105391. Xiaoqing Jin acknowledges the support from the Fundamental Research Funds for the Central Universities (No. CDJZR14285501).

## Appendix A. Detailed expressions of the $G$ functions

Detailed expressions of the  $G$  functions were derived by Jin et al. (2011), which are listed as follows for convenience in use.

$$G_M^{(1)}(\lambda) = J_M(\lambda) \quad (\text{A.1})$$

$$G_{MN}^{(2)}(\lambda) = \frac{1}{2(1-\nu)} [a_M^2 J_{MN} - J_M(\lambda)] = G_{NM}^{(2)} \quad (\text{A.2})$$

$$G_M^{(3)}(\lambda) = \frac{\rho_1(\lambda)\rho_2(\lambda)\rho_3(\lambda)}{2(1-\nu)} [1 - \rho_M^2(\lambda)] \quad (\text{A.3})$$

$$G_{ijkl}^{(4)} = -\frac{\rho_1(\lambda)\rho_2(\lambda)\rho_3(\lambda)}{2} \left( \delta_{ik}n_jn_l + \delta_{il}n_jn_k + \delta_{jk}n_in_l + \delta_{jl}n_in_k + \frac{2\nu}{1-\nu} \delta_{kl}n_in_j \right) \quad (\text{A.4})$$

$$G_{ijkl}^{(5)}(\lambda) = \frac{\rho_1(\lambda)\rho_2(\lambda)\rho_3(\lambda)}{1-\nu} [\rho_l^2(\lambda) + \rho_j^2(\lambda) + \rho_k^2(\lambda) + \rho_i^2(\lambda)] \quad (\text{A.5})$$

$$G^{(6)}(\lambda) = \frac{\rho_1(\lambda)\rho_2(\lambda)\rho_3(\lambda)}{2(1-\nu)} [\rho_m(\lambda)\rho_n(\lambda) - 4\rho_M^2(\lambda)n_mn_n - 5] \quad (\text{A.6})$$

where

$$\rho_M(\lambda) = \frac{a_M}{\sqrt{a_M^2 + \lambda}}$$

Variable  $a_M$  is the semi-major-axis of the ellipsoidal inclusion. Functions  $J_M$  and  $J_{MN}$  in above equations are related to the  $I$ -integrals in the work of Mura (1993) as follows.

$$J_M(\lambda) = \frac{1}{4\pi} I_M; \quad J_{MN}(\lambda) = \frac{1}{4\pi} I_{MN}$$

## References

- Bartels, R.H., Golub, G.H., 1969. The simplex method of linear programming using LU decomposition. *Commun. ACM* 12, 266–268.
- Chapman, S.J., 2004. Fortran 90/95 for Scientists and Engineers. McGraw-Hill Higher Education.
- Chiu, Y.P., 1977. On the stress field due to initial strains in a cuboid surrounded by an infinite elastic space. *ASME J. Appl. Mech.* 44, 587–590.
- Eshelby, J.D., 1957. The determination of the elastic field of an ellipsoidal inclusion, and related problems. *Proc. R. Soc. A* 241, 376–396.
- Eshelby, J.D., 1959. The elastic field outside an ellipsoidal inclusion. *Proc. R. Soc. A* 252, 561–569.
- Gong, S.X., Meguid, S.A., 1993. On the elastic fields of an elliptical inhomogeneity under plane deformation. *Proc. R. Soc. A* 443, 457–471.
- Greco, A., Martini, A., Liu, Y., Lin, C., Wang, Q.J., 2010. Rolling contact fatigue performance of vibro-mechanical textured surfaces. *Tribol. Trans.* 53, 610–620.
- Horii, H., Nemat-Nasser, S., 1985. Elastic fields of interacting inhomogeneities. *Int. J. Solids Struct.* 21, 731–745.
- Jin, X., Keer, L.M., Wang, Q., 2009. New Green's function for stress field and a note of its application in quantum-wire structures. *Int. J. Solids Struct.* 46, 3788–3798.
- Jin, X., Keer, L.M., Wang, Q., 2011. A closed-form solution for the Eshelby tensor and the elastic field outside an elliptic cylindrical inclusion. *ASME J. Appl. Mech.* 78, 031009.
- Jin, X., Wang, Z., Zhou, Q., Keer, L.M., Wang, Q., 2014. On the solution of an elliptical inhomogeneity in plane elasticity by the equivalent inclusion method. *J. Elast.* 114, 1–18.
- Ju, J., Sun, L., 1999. A novel formulation for the exterior-point Eshelby's tensor of an ellipsoidal inclusion. *ASME J. Appl. Mech.* 66, 570.
- Kuo, C.H., 2007. Stress disturbances caused by the inhomogeneity in an elastic half-space subjected to contact loading. *Int. J. Solids Struct.* 44, 860–873.
- Kushch, V., Shmegeera, S., Buryachenko, V., 2005. Interacting elliptic inclusions by the method of complex potentials. *Int. J. Solids Struct.* 42, 5491–5512.
- Leroux, J., Fulleringer, B., Nélías, D., 2010. Contact analysis in presence of spherical inhomogeneities within a half-space. *Int. J. Solids Struct.* 47, 3034–3049.
- Leroux, J., Nélías, D., 2011. Stick-slip analysis of a circular point contact between a rigid sphere and a flat unidirectional composite with cylindrical fibers. *Int. J. Solids Struct.* 48, 3510–3520.
- Li, P., Wang, Z., Li, X., Jin, X., Wayne Chen, W., Li, Y., Jane Wang, Q., 2013. Elastoplastic indentation of a half-space by a rigid sphere under normal and torque loading. *Tribol. Int.* 62, 141–148.
- Liu, S., Jin, X., Wang, Z., Keer, L.M., Wang, Q., 2012. Analytical solution for elastic fields caused by eigenstrains in a half-space and numerical implementation based on FFT. *Int. J. Plast.* 35, 135–154.
- Liu, S., Wang, Q., 2002. Studying contact stress fields caused by surface tractions with a discrete convolution and fast Fourier transform algorithm. *ASME J. Tribol.* 124, 36.
- Liu, S., Wang, Q., Liu, G., 2000. A versatile method of discrete convolution and FFT (DC-FFT) for contact analyses. *Wear* 243, 101–111.
- Liu, S., Wang, Q.J., 2005. Elastic fields due to eigenstrains in a half-space. *ASME J. Appl. Mech.* 72, 871–878.
- Meguid, S.A., Zhu, Z.H., 1995. Stress distribution in dissimilar materials containing inhomogeneities near the interface using a novel finite element. *Finite Elem. Anal. Des.* 20, 283–298.
- Moschovidis, Z.A., Mura, T., 1975. Two-ellipsoidal inhomogeneities by the equivalent inclusion method. *ASME J. Appl. Mech.* 42, 847–852.
- Mura, T., 1993. *Micromechanics of Defects in Solids*, second ed. Kluwer Academic, Dordrecht.

- Murakami, Y., Endo, M., 1994. Effects of defects, inclusions and inhomogeneities on fatigue strength. *Int. J. Fatigue* 16, 163–182.
- Muskhelishvili, N.I., 1953. *Some Basic Problems of the Mathematical Theory of Elasticity*. Cambridge Univ Press.
- Polonsky, I., Keer, L., 1999. A numerical method for solving rough contact problems based on the multi-level multi-summation and conjugate gradient techniques. *Wear* 231, 206–219.
- Shabana, A.A., 2005. *Dynamics of Multibody Systems*. Cambridge University Press.
- Shodja, H., Roumi, F., 2005. Overall behavior of composites with periodic multi-inhomogeneities. *Mech. Mater.* 37, 343–353.
- Singh, I.V., Mishra, B.K., Bhattacharya, S., 2011. XFEM simulation of cracks, holes and inclusions in functionally graded materials. *Int. J. Mech. Mater. Des.* 7, 199–218.
- Wang, Z., Jin, X., Keer, L.M., Wang, Q., 2012a. A numerical approach for analyzing three-dimensional steady-state rolling contact including creep using a fast semi-analytical method. *Tribol. Trans.* 55, 446–457.
- Wang, Z., Jin, X., Keer, L.M., Wang, Q., 2012b. Numerical methods for contact between two joined quarter spaces and a rigid sphere. *Int. J. Solids Struct.* 49, 2515–2527.
- Wang, Z., Jin, X., Keer, L.M., Wang, Q., 2013a. Novel model for partial-slip contact involving a material with inhomogeneity. *ASME J. Tribol.* 135, 041401.
- Wang, Z.J., Jin, X.Q., Zhou, Q.H., Keer, L.M., Wang, Q., 2013b. An efficient numerical method with a parallel computational strategy for solving arbitrarily shaped inclusions in elastoplastic contact problems. *ASME J. Tribol.* 135, 031401.
- Wu, L., Du, S., 1995a. The elastic field caused by a circular cylindrical inclusion. I: Inside the region  $x_{12} + x_{22} < a^2$ ,  $-\infty < x_3 < \infty$  where the circular cylindrical inclusion is expressed by  $x_{12} + x_{22} \leq a^2$ ,  $-h \leq x_3 \leq h$ . *ASME J. Appl. Mech.* 62, 579–584.
- Wu, L., Du, S., 1995b. The elastic field caused by a circular cylindrical inclusion. II: Inside the region  $x_{12} + x_{22} > a^2$ ,  $-\infty < x_3 < \infty$  where the circular cylindrical inclusion is expressed by  $x_{12} + x_{22} \leq a^2$ ,  $-h \leq x_3 \leq h$ . *ASME J. Appl. Mech.* 62, 585–589.
- Yu, J.H., Kuang, Z.B., 2003. The stress analysis of an ellipsoidal inhomogeneity in dissimilar media. *Compos. Sci. Technol.* 63, 955–966.
- Zaretsky, E.Y., 1987. Fatigue criterion to system design, life, and reliability. *J. Propul. Power* 3, 76–83.
- Zhou, K., Chen, W.W., Keer, L.M., Ai, X., Sawamiphakdi, K., Glaws, P., Wang, Q.J., 2011a. Multiple 3D inhomogeneous inclusions in a half space under contact loading. *Mech. Mater.* 43, 444–457.
- Zhou, K., Chen, W.W., Keer, L.M., Wang, Q.J., 2009. A fast method for solving three-dimensional arbitrarily shaped inclusions in a half space. *Comput. Methods Appl. Mech.* 198, 885–892.
- Zhou, K., Keer, L.M., Wang, Q.J., 2011b. Semi-analytic solution for multiple interacting three-dimensional inhomogeneous inclusions of arbitrary shape in an infinite space. *Int. J. Numer. Methods Eng.* 87, 617–638.
- Zhou, K., Keer, L.M., Wang, Q.J., Ai, X., Sawamiphakdi, K., Glaws, P., Paire, M., Che, F., 2012. Interaction of multiple inhomogeneous inclusions beneath a surface. *Comput. Methods Appl. Mech.* 217–220, 25–33.
- Zhou, Q., Jin, X., Wang, Z., Wang, J., Keer, L.M., Wang, Q., 2014. Numerical implementation of the equivalent inclusion method for 2D arbitrarily shaped inhomogeneities. *J. Elast.* <http://dx.doi.org/10.1007/s10659-014-9477-2>.